Invited Paper

Diffraction-limited beams and their applications for ultrasonic imaging and tissue characterization

Jian-yu Lu and James F. Greenleaf

Biodynamics Research Unit, Department of Physiology and Biophysics, Mayo Clinic/Foundation, Rochester, MN 55905

ABSTRACT

Diffraction-limited beams were first discovered by Durnin in 1987. These beams are pencil-like and have very large depth of field. Recently, we have discovered new families of diffraction-limited beams which contain some of the diffraction-limited beams known previously, such as, the plane wave and Durnin's Bessel beams, in addition to an infinite variety of new beams, such as X waves. In this paper, we generalize the new diffraction-limited beams to n-dimensional space, review the recent development of the diffraction-limited beams, and describe their applications to medical ultrasonic imaging, tissue characterization and nondestructive evaluation of materials. Advantages and disadvantages of these beams are discussed and their possible applications to other wave related fields are addressed.

1. INTRODUCTION

Diffraction-limited beams are represented by a class of solutions to wave equations. They are propagation-invariant or almost propagation-invariant if produced with a finite aperture. The dependence of their structure on variables z and t are in the form of $z - c_1 t$, where z, c_1 and t are distance along propagation direction, speed of waves, and time, respectively. In 1987, Durnin[1] discovered the first diffraction-limited beams which he termed, "nondiffracting beams or diffraction-free beams." These beams were represented by Bessel solutions of the sourceless, loss-less, and isotropic/homogeneous scalar Helmholtz equation. Unlike conventional diffracting beams, these new beams could propagate to infinite distance without any changes of their lateral intensity profiles provided that they were produced over an infinite aperture with infinite energy. Since Durnin's discovery, great effort has been devoted to development of new diffraction-limited or well-collimated beams in optics.[2-8] Experiments have also been performed to produce the diffraction-limited beams with optical devices.[2]

In addition to the development of diffraction-limited beams in optics, Brittingham[9] discovered electromagnetic localized waves in 1983. These localized waves were termed as Focus Wave Modes, and they are pulses which propagate at the speed of light to infinite distance in free space with only local deformations. Initiated by Brittingham's work, Ziolkowski[10] developed a new Focus Wave Mode in 1985. Taking the Focus Wave Mode as a basis, Ziolkowski constructed new localized waves, such as the Modified Power Spectrum pulse,[11] using Laplace transform methods. Acoustic experiments were carried out by Ziolkowski et al.[11-12] to produce Modified Power Spectrum pulses. Generalization and further detailed analysis of localized waves have been reported.[13-18] Possible applications of the localized waves

0-8194-0906-5/92/$4.00

to energy transmission and private communication were also addressed by Ziolkowski.[16] In addition, the localized wave solutions have been used to explain the fundamental characteristics of the photon which presents mysterious wave-particle duality.[19] Localized solutions were also derived for the schrodinger, Klein-Gorden, and Dirac equations which represent nonrelativistic or relativistic particles.[19-20]

Following the optical development of diffraction-limited beams, several people have explored the acoustic production of these beams. Hsu et al.[21] have made the first narrow-band diffraction-limited ultrasonic transducer using nonuniform poling of a lead zirconate-titanate (PZT) ceramic and produced a J_0 Bessel beam in water. Campbell et al.[22] have studied theoretically the broadband production of a finite aperture J_0 Bessel diffraction-limited beam. Lu and Greenleaf[23-34] have produced broadband J_0 Bessel beams in acoustic experiments and applied them to medical ultrasonic imaging, tissue characterization, and nondestructive evaluation of materials. Processing of images obtained with the J_0 Bessel beam has also been studied and simplified procedures for restoration of images demonstrated using the nonspreading property of diffraction-limited beams.[33,35]

Recently, Lu and Greenleaf[26-28] discovered families of generalized solutions to the loss-less, isotropic/homogeneous scalar wave equation. These solutions include some of the diffraction-limited beams known previously, such as Durnin's beams and the plane wave, in addition to an infinite variety of new beams. One family of the new diffraction-limited beams are of particular interest and were termed "X waves" because they have an X-like shape in a plane along the axial axis of the waves. A zeroth-order X wave has been produced in water with a broadband ultrasonic annular array transducer made of PZT ceramics/polymer composites.[28] Theoretically X waves maintain their complex waveform without changing (nonspreading) in any direction as they propagate to infinite distance in loss-less isotropic/homogeneous media provided that they are produced with an infinite aperture and energy. Even when they are produced with finite aperture and energy, X waves have very large depth of field and can be produced with practical bandwidths. Since X waves are nonspreading, they hold more promise for imaging and tissue characterization applications than broadband Bessel beams which spread along the propagation axis as they propagate.[22,25]

In this paper, we present a generalization of diffraction-limited beams to n-dimensional space and review some applications of diffraction-limited beams in medical ultrasonic imaging, tissue characterization and nondestructive evaluation of materials. In Section 2, we derive n-dimensional diffraction-limited beams and give some examples for various n. Experiments with a J_0 Bessel beam and a zeroth-order X wave in water with a finite aperture ultrasonic annular array transducer are described in Section 3. In Section 4, we review applications of diffraction-limited beams (for example, the J_0 Bessel beam) in medical ultrasonic imaging, biological tissue characterization and nondestructive evaluation of materials. Sections 5 and 6 provide a discussion, and conclusion, respectively.

2. N-DIMENSIONAL DIFFRACTION-LIMITED BEAMS

Many physical phenomena (such as those in acoustics, optics, and electromagnetics) are governed by wave equations. In this section, we will obtain diffraction-limited solutions for an n-dimensional wave equation and give examples for various dimensions, n.

2.1. Wave equation

A source-free loss-less n-dimensional isotropic/homogeneous scalar wave equation in rectangular coordinates is given by[36]

$$\left[\sum_{j=1}^{n}\frac{\partial^2}{\partial x_j^2}-\frac{1}{c^2}\frac{\partial^2}{\partial t^2}\right]\Phi=0, \tag{1}$$

where x_j, $(j=1,2,\cdots,n)$, represent rectangular coordinates in n-dimensional space, t is time, n is an integer, c is a constant, and $\Phi=\Phi(x_1,x_2,\cdots,x_n;t)$ is an n-dimensional wave field.

2.2. One of the special families of solutions

One of the special families of solutions of the n-dimensional wave equation (Eq. (1)) is given by

$$\Phi(x_1,x_2,\cdots,x_n;t)=f(s), \tag{2}$$

where

$$s=\sum_{j=1}^{n}D_jx_j-Et,\ \ (n\geq 1), \tag{3}$$

and where

$$E=\pm c\sqrt{\sum_{j=1}^{n}D_j^2},\ \ (n\geq 1). \tag{4}$$

The D_j are complex coefficients which could relate to the jth component of an n-dimensional vector wave number and are independent of the spatial and time variables (x_j $(j=1,2,\cdots,n)$ and t), and $f(s)$ is any complex function (well-behaved) of s.

If $n=0$, f(s) is only a function of time, t, and will not represent a wave. Therefore, in the following, we discuss only the cases where $n\neq 0$.

Eq. (3) can be rewritten as

$$s=\sum_{j=1}^{n-1}D_jx_j+D_n(x_n-c_1t),\ \ (n\geq 1), \tag{5}$$

where

$$c_1 = E/D_n = \pm c\sqrt{1 + \sum_{j=1}^{n-1} D_j^2/D_n^2}, \quad (n \geq 1). \tag{6}$$

2.3. Diffraction-limited solutions

If c_1 in Eq. (5) is real, f(s) represents a diffraction-limited wave propagating along axis, x_n, at the phase velocity of c_1, in an n-dimensional space, i.e., traveling with the wave, one sees a complex wave pattern unchanged in amplitude and phase. The "$\pm$" term in Eq. (6) represents forward and backward propagating waves, respectively. In the following, we consider forward going waves only. For backward going waves, the results are similar.

In a manner similar to that used in Reference 27, an infinite variety of new diffraction-limited waves, which are also exact solutions of Eq. (1), can be constructed by linear superposition of f(s) over any free parameters that associate with the coefficients, D_j, $(j = 1, 2, \cdots, n)$ in the n-dimensional space $(n \geq 1)$ as long as the speed, c_1, is independent of these parameters.

We now describe a few specific members of this family of solutions (Eqs. (2) to (4)) in different dimensions, n.

2.3.1. Three-dimensional diffraction-limited waves (example: X waves)

If $n = 3, x_1 = x$, $x_2 = y$, and $x_3 = z$, Eq. (1) is a three-dimensional wave equation. Assume that $D_1 = \alpha_0(k, \zeta)\cos\theta$, $D_2 = -\alpha_0(k, \zeta)\sin\theta$, and $D_3 = b(k, \zeta)$, where θ, k and ζ are free parameters which are independent of the spatial position, $\vec{r} = (x, y, z)$, and time, t, and $\alpha_0(k, \zeta)$ and $b(k, \zeta)$ are any well-behaved complex functions of k and ζ. From Eq. (5), we obtain

$$s = \alpha_0(k, \zeta)x\cos\theta - \alpha_0(k, \zeta)y\sin\theta + b(k, \zeta)(z - c_1 t), \tag{7}$$

where

$$c_1 = c\sqrt{1 + \alpha_0^2(k, \zeta)/b^2(k, \zeta)}. \tag{8}$$

Integrating $f(s)$ (see Eq. (2)) over free parameters k and θ, we obtain[27]

$$\Phi_{3\zeta}(s) = \int_0^\infty T(k)\left[\frac{1}{2\pi}\int_{-\pi}^{\pi} A(\theta)f(s)d\theta\right]dk, \tag{9}$$

where the subscript "3" means "three-dimensional," $T(k)$ is any well-behaved complex function of k, and $A(\theta)$ represents any well-behaved complex weighting function of the integration with respect to θ.

Letting $\alpha_0(k,\zeta) = -ik\sin\zeta$, $b(k,\zeta) = ik\cos\zeta$, $f(s) = e^s$, $A(\theta) = i^m e^{im\theta}$, and $T(k) = B(k)e^{-a_0 k}$, and using an integral representation of the Bessel functions,[37] we obtain from Eq. (9) the generalized diffraction-limited X wave solution (mth-order X waves)[27]

$$\Phi_{X_m} = e^{im\phi}\int_0^\infty B(k)J_m(kr\sin\zeta)e^{-k[a_0 - i\cos\zeta(z-c_1 t)]}dk, \quad (m = 0,\ 1,\ 2, ...), \tag{10}$$

which is the Laplace transform of the function, $B(k)J_m(kr\sin\zeta)$, where $B(k)$ is any well-behaved complex function of k and is a temporal frequency transfer function of a radiator system, J_m is the mth-order Bessel function of the first kind, $c_1 = c/\cos\zeta$ is the phase speed of the diffraction-limited X waves, $a_0 > 0$ is a constant, and $r = \sqrt{x^2 + y^2}$ and ϕ are variables of polar coordinates.

2.3.2. Two-dimensional diffraction-limited waves (example: oblique plane waves)

A two-dimensional diffraction-limited wave can be obtained if we let $n = 2$, $x_1 = x$, and $x_2 = z$. From Eqs. (5) and (6) we have

$$s = D_1 x + D_2(z - c_1 t), \tag{11}$$

where

$$c_1 = c\sqrt{1 + D_1^2/D_2^2}. \tag{12}$$

Let $D_1 = D_1(k,\zeta)$ and $D_2 = D_2(k,\zeta)$, we obtain from Eq. (11)

$$f(s) = f(D_1(k,\zeta)x + D_2(k,\zeta)(z - c_1 t)), \tag{13}$$

where k and ζ are free parameters which are independent of the spatial and time variables (x, z, and t).

Integrating $f(s)$ over k or ζ, we obtain two families of solutions to the two-dimensional wave equation

$$\Phi_{2\zeta} = \int_0^\infty T(k)f(s)dk = \int_0^\infty T(k)f(D_1(k,\zeta) + D_2(k,\zeta)(z - c_1 t))dk, \tag{14}$$

and

$$\Phi_{2k} = \int_{-\pi}^{\pi} D(\zeta)f(s)d\zeta = \int_{-\pi}^{\pi} D(\zeta)f(D_1(k,\zeta) + D_2(k,\zeta)(z - c_1 t))d\zeta, \tag{15}$$

where the subscript "2" means "two-dimensional," $T(k)$ and $D(\zeta)$ are any well-behaved complex functions of k and ζ. These families of solutions (Eqs. (14) and (15)) also represent diffraction-limited waves if c_1 in Eq. (12) is real and independent of k or ζ.

We obtain oblique plane waves if in Eq. (14) we let $D_1(k,\zeta) = ik\sin\zeta$, $D_2(k,\zeta) = ik\cos\zeta$, and $f(s) = e^s$

$$\Phi_{OP} = \int_0^\infty T(k)e^{ikx\sin\zeta + ik\cos\zeta(z-c_1t)}dk, \tag{16}$$

where the subscript "OP" represents "oblique plane waves," $c_1 = c/\cos\zeta$, and ζ represents an angle between the propagation direction and the axis, z. Let $T(k) = B(k)e^{-a_0k}$, where $B(k)$ is any well-behaved complex function of k, Eq. (16) is a Laplace transform of the function, $B(k)e^{ikx\sin\zeta}$, and is given by

$$\Phi_{OP} = \int_0^\infty \left[B(k)e^{ikx\sin\zeta}\right]e^{-k[a_0 - i\cos\zeta(z-c_1t)]}dk. \tag{17}$$

If $B(k) = a_0$, a Laplace transform table gives,[38]

$$\int_0^\infty e^{-ak}e^{-sk}dk = \frac{1}{s+a}, \quad R_e\{s\} > -R_e\{a\}, \tag{18}$$

resulting in broadband oblique plane waves

$$\Phi_{OPBB} = \frac{a_0}{a_0 - i[x\sin\zeta + \cos\zeta(z-c_1t)]}, \quad a_0 > 0, \tag{19}$$

where the subscript "BB" means "broadband." If $B(k)$ is a band-limited function, band-limited oblique plane waves are obtained

$$\Phi_{OPBL} = \frac{1}{a_0}\mathcal{F}^{-1}\left[B\left(\frac{\omega}{c}\right)\right] * \Phi_{OPBB}, \tag{20}$$

where the subscript "BL" means "band-limited" and "*" represents convolution with respect to time, t.

The real part of Eq. (19) is given by

$$R_e\{\Phi_{OPBB}\} = \frac{1}{1 + \left[x\frac{\sin\zeta}{a_0} + \frac{\cos\zeta}{a_0}(z-c_1t)\right]^2}, \quad a_0 > 0, \tag{21}$$

which has a peak ($\equiv 1$) along the line $(z - c_1t) = x\tan(-\zeta)$.

2.3.3. One-dimensional diffraction-limited waves (example: plane waves)

If $n = 1$, and $x_1 = z$, from Eqs. (5) and (6), we have

$$s = D_1(z - c_1t), \tag{22}$$

and

$$c_1 = c, \tag{23}$$

obtaining plane waves that travel in the positive z direction at speed of sound, c with the pulse waveforms

$$f(s) = f(D_1(z - ct)). \tag{24}$$

Obviously, the plane waves are diffraction-limited and are solutions of Eq. (1) with $n = 1$. Let $D_1 = ik$, where $k = \omega/c$ (ω is an angular frequency) is a wave number, and $f(s) = e^s$, obtaining a CW plane wave

$$f(s) = e^{ik(z-ct)}. \tag{25}$$

If $D_1 = 1$, and $f(s) = e^{s^2/\sigma^2}$, Eq. (24) represents a plane wave with a pulse of Gaussian temporal shape transmitted from an infinite plane source which is independent of spatial coordinates, x and y

$$\Phi_G = f(s) = e^{(z-ct)^2/\sigma^2}, \tag{26}$$

where σ is a constant which represents the waist of the Gaussian weighted pulse.

In next section, we will show some of the diffraction-limited beams produced in water with a finite aperture/bandwidth transducer. They are good approximations of the above theoretical diffraction-limited beams over large axial distances (depth of field).

3. PRODUCTION OF DIFFRACTION-LIMITED BEAMS IN WATER WITH FINITE APERTURE

3.1. J_0 Bessel beam

The J_0 Bessel beam can be derived from Eq.(10). Let $B(k) = e^{k_0 a_0}\delta(k - k_0)$, $m = 0$ and $k_0 \sin\zeta = \alpha$, where δ is the Dirac-Delta function, $k_0 = 2\pi f_0/c$, f_0 is frequency, c is speed of sound of media in which the beam propagates, and α is a constant which is a lateral scaling factor of a Bessel function, obtaining the J_0 Bessel beam[1]

$$J_0(\alpha r)e^{i\beta z - i\omega t}, \tag{27}$$

where $\omega = 2\pi f_0$ is an angular frequency and $\beta = \sqrt{k_0^2 - \alpha^2}$.

In practice, the J_0 Bessel beam can only be produced with a finite aperture. If the radius of the aperture is a, the depth of field of the J_0 Bessel beam is given by[1]

$$Z_{Bmax} = a\sqrt{\left(\frac{\omega}{\alpha c}\right)^2 - 1}. \tag{28}$$

This equation is accurate only for $Z_{Bmax} < \pi a^2/\lambda$ where $\pi a^2/\lambda$ is the Rayleigh distance and λ is the wavelength of the beam.

Figures 1 and 2 show narrow band and broadband J_0 Bessel beams measured in water. They were produced with an ultrasonic annular array transducer. The transducer has a diameter of 50 mm and 10 annular elements. The width of each annular element is designed to be equal to a lobe of the J_0 Bessel function with $\alpha = 1202.45m^{-1}$, i.e., the width of all the lobes are constants and independent of frequency. The transducer is made of PZT ceramics/polymer composite with a central frequency of 2.5 MHz. The bandwidth of the transducer is about 50% of its central frequency. To drive the transducer, 10 transmitting electrical circuits were developed. The output voltage of each circuit was adjusted such that the pressure produced by each transducer element at the surface of the transducer was proportional to the peak (positive or negative) of the corresponding lobe of the J_0 Bessel function.

To produce the CW beam in Fig. 1, a 2.5 MHz $200\mu s$ tone burst was used. The beam was measured in a plane along the central axis from 5 mm to 205 mm away from the surface of the transducer. The panel size in Fig. 1 is 48 mm $\times$ 200 mm.

The upper-left panel of Fig. 1 shows the analytic envelope of the measured rf signals. The upper-right, lower-left and lower-right panels of Fig. 1 represent log compressed, -6 dB clipped log compressed and -12 dB clipped log compressed envelope.[1]

The images in Fig. 2 were produced with the same transducer and electronic circuits as those used for Fig. 1, but a broadband electrical pulse (about one and half cycles of a sinusoidal wave) was used to drive the transducer approximated by,

$$e^{-t^2/t_0^2} \sin(2\pi f_0 t) \tag{29}$$

where f_0 = 2.5 MHz, $t_0 = 0.4\mu s$.

Figure 3 is the lateral and axial line plots of the pulses in Fig. 2. The broadband J_0 Bessel beam produced with a finite aperture maintains a constant main beamwidth (lateral characteristics) throughout the depth of field (the depth of field the J_0 Bessel beam in water calculated from Eq. (28) is about 216 mm, and its -6 dB main beamwidth is about 2.53 mm[23]).

3.2. Zeroth-order X wave

Substituting m = 0 into Eq. (10) and using a Laplace transform table[38], we obtain the zeroth-order X wave[27]

$$\frac{1}{a_0} b(t) * \frac{a_0}{\sqrt{(r\sin\zeta)^2 + [a_0 - i\cos\zeta(z - c_1 t)]^2}} \tag{30}$$

[1] (The envelope image was log compressed with the formula $20\log_{10}(x)$, where x represents a pixel of the envelope image which was normalized to 1 to 255, and "$-$x dB clipped" means that only 0 dB to $-$x dB of the log compressed images are displayed (from white to black)).

where $b(t)$ is an impulse response of the transducer (inverse Fourier transform of the transfer function $B(k)$) and "*" represents convolution with respect to time.

The depth of field of the X wave is given by[27]

$$Z_{Xmax} = a \cot \zeta, \tag{31}$$

where ζ is an axicon angle[39] of the X waves and aperture radius is a. Eq. (31) is accurate only for $Z_{Xmax} < \pi a^2/\lambda$, where λ is the central wavelength of the X waves. (For extremely wide-band pulses, the Rayleigh distance concept does not apply. In this case, we can only say that for Eq. (31) to be valid, ζ must not be so small that the zeroth-order X wave becomes virtually a plane wave.)

Figure 4 shows simulated and measured zeroth-order X wave pulses at distances 170 mm and 340 mm, respectively, away from the surface of the transducer. The transducer used was the same as that for producing the J_0 Bessel beam. In the simulation, the transmitting transfer function of the transducer ($B(k)$) was assumed to be the Blackman window function[44] peaked at 2.5 MHz and with a -6 dB bandwidth around 2.1 MHz. The drive waveform for each transducer element was calculated from Eq. (30) by setting $B(k) = a_0 = 0.05mm$, $z = 0mm$, $\zeta = 4^o$, and r as the average radius of that element. The upper two panels are simulated (with an exact X wave aperture weighting) analytic envelopes of the real part of the X wave pulses, and the lower two show the experimentally measured results. The transducer is assumed to be on the right-hand side of each panel and the panel size is 25 mm $\times$ 10 mm.

Although the zeroth-order X wave has very low sidelobes in lateral and axial directions (Fig. 5), it does have higher sidelobes along its X branches (Fig. 6) (in Fig. 6, the line plots represent the field magnitude along the largest X branches versus the lateral distance, r).

The depth of field of the zeroth-order X wave calculated from Eq. (31) is about 358 mm in water and its -6 dB lateral and axial beam widths are about 4.7 mm and 0.65 mm, respectively.

The diffraction-limited beams can be almost exactly produced with finite apertures and energy over very large depth of field as seen from the above study. These beams have small main beam width and are pencil-like or bullet-like in loss-less, isotropic/homogeneous media.

4. APPLICATION OF DIFFRACTION-LIMITED BEAMS

Because the diffraction-limited beams are nonspreading over large depth of field, they could have many applications in various wave related fields, such as acoustics, optics, microwaves and elctromagnetics. In this section, we give a few examples of the applications of the diffraction-limited beams in ultrasonic imaging and biological tissue characterization.

4.1. Application for medical imaging

Conventionally, focused beams are used for medical pulse-echo imaging. These beams have short depth of field, especially, for shorter focal lengths. One technique to achieve a large depth of field using a focused beam is the use of multiple transmit focusing. This technique uses multiple transmitted beams of different focal depths. For each focal depth, a strip of image is recorded and montaged with other strips to form a full frame of image. This procedure reduces the imaging frame rate (by a factor of the number of the image strips), causes possible spatial misalignment of the objects and results in blurred images of moving objects such as the heart. The low imaging frame rate might even have influence on diagnosis of stationary organs because the images are distorted or become discontinuous as physicians move the probes (transducers) to find tumors and other masses.

Because of the small main beamwidth and large depth of field of the diffraction-limited beams, high-resolution and high-frame rate images can be obtained over entire region of interest. Figure 7 shows a B-scan image of a commercial RMI413A tissue equivalent phantom (attenuation coefficient of the phantom is about 0.7 dB/MHz/cm) obtained with the J_0 Bessel beam (see Fig. 2) which was used in both transmitting and receiving.[25] This image is compared to Fig. 8 where a focused Gaussian beam was used in both transmitting and receiving to obtain the B-scan image. The focused Gaussian beam was produced with the same transducer as that used for producing the J_0 Bessel beam but the elements of the transducer were weighted by a Gaussian function. The full width at half maximum (FWHM) of the Gaussian function at the surface of transducer was 25 mm and the focal length of the Gaussian beam was fixed and was about 120 mm.

The large depth of field of the J_0 Bessel beam (Fig. 7) compares favorably to the strong depth dependent image of the conventional focused Gaussian beam (Fig. 8) demonstrating the robustness of the J_0 Bessel beam for medical imaging.

4.2. Application for biological tissue characterization

Since the diffraction-limited beams do not spread as they propagate over large depth of field, corrections for transducer beam diffraction in tissue characterization would be minimal. In addition, the nonspreading property of diffraction-limited beams would provide a relatively constant sampling volume over depth and, therefore, changes of statistical measure of backscattered signals reflect only alterations in the spatial distribution of scatterers, resulting in consistent estimations of tissue parameters over large depth. Estimation of backscatter coefficient with a diffraction-limited beam is presented in the following.

Backscatter coefficients of biological soft tissues have been studied extensively with conventional beams.[40-42] The conventional formula for estimating the backscatter coefficient at an angular frequency,

ω_0, is given by[40]

$$\eta(\omega_0)\xrightarrow[\tau \text{ increasing}]{} \frac{\overline{\left|\tilde{V}_s(\omega_0)\right|^2}}{\left(\frac{\tau}{2\pi}\right)^2 \int\int_{\Omega}\int d\vec{r'}\left\|J'_{\omega_0}\left(\vec{r'}\right)\right\|^2} \tag{32}$$

where η_{ω_0} is the backscatter coefficient calculated at the angular frequency $\omega = \omega_0$, $\overline{|V_s(\omega_0)|^2}$ is an ensemble average of the modulus square of Fourier transform of back-scattered signals calculated at ω_0, τ is width of a time gate applied to the back-scattered signals, Ω defines a scattering volume interrogated by the incident wave, $J'_{\omega_0}\left(\vec{r'}\right)$ is given by

$$J'_{\omega_0}\left(\vec{r'}\right) \equiv 2\pi \int_{-\infty}^{\infty} d\omega' T\left(\omega'\right) B_0\left(\omega'\right) \frac{e^{-j\left(\omega_0-\omega'\right)\tau}-1}{-j(\omega_0-\omega')\tau} e^{-j\left(\omega_0-\omega'\right)t_0}\left[\left(j\lambda U\left(\vec{r},\omega'\right)\right)^*\right]^2|_{t_0=2r_p/c} \tag{33}$$

where $T(\omega)B_0(\omega)$ is a system transfer function of the transducer which includes the spectrum of the electrical excitation pulse, and the transmitting and receiving transfer functions of the transducer (it could be determined experimentally with a reference reflector[40]), λ is wavelength, $U(\vec{r},\omega)$ is a complex wave field at position $\vec{r}$ and angular frequency ω, r_p is the nearest distance between the transducer and the sampling volume, c is the speed of sound of the scattering medium and "*" represents a complex conjugate.

With a finite aperture J_0 Bessel beam (axially symmetric), if $(\omega_0/c)^2 \gg \alpha^2$ (a condition for using the inverse Fourier transform), Eq. (32) can be simplified[24]

$$\eta(\omega_0)\xrightarrow[\tau \text{ increasing}]{} \frac{\overline{\left|\tilde{V}_s(\omega_0)\right|^2}}{\frac{(2\pi)^7\tau^2c^5}{2}\int_0^a r dr J_0^4(\alpha r)\int_0^{\tau} dt\left|\mathcal{F}^{-1}\left\{T^*(\omega')B_0^*(\omega')\frac{e^{j\left(\omega_0-\omega'\right)\tau}-1}{\left(\omega_0-\omega'\right)\tau\omega'^2}\right\}(t)\right|^2} \tag{34}$$

where $\mathcal{F}^{-1}$ is the inverse Fourier transform and a is the radius of the transducer.

A great reduction of computation is obtained in Eq. (34). Eq. (34) needs only two one-dimensional integrations in addition to one inverse Fourier transform, while in Eq. (32), four-dimensional integrations for various transducer-scattering volume distances are required when using an axially symmetric focused beam. Experimental results for estimating the backscatter coefficients of an excised human liver sample and a commercial RMI413A tissue equivalent phantom using both diffraction-limited beam and conventional focused Gaussian beam have been reported.[24] Not only was the computation reduced, but the estimation was more depth independent with the diffraction-limited beam (the J_0 Bessel beam).

4.3. Application for nondestructive evaluation of materials

Pulse-echo imaging is one of the methods used in nondestructive evaluation of materials.[43] When a non-focused transducer is used for pulse-echo imaging, the lateral resolution of the images is poor

because of the wide main beam width of the non-focused beams. Although non-focused beams or point sources can be used in synthetic aperture imaging to improve resolution, data acquisition and image reconstruction procedures involved are complex. To improve image resolution without using complicated data acquisition and image reconstruction, focused beams can be used. However, the focal length of a focused beam changes with the speed of sound of the materials inspected. This complicates procedures for evaluating materials of various speeds of sound. In addition, the depth of field of the focused beams are usually short, which means that the high-lateral resolution images of flaws can only be obtained near the depth of focus.

Diffraction-limited beams such as Bessel beams and X waves maintain their beam shape in loss-less, isotropic/homogeneous media. They are naturally focused in flat materials of any speed of sound and have a narrow main beam width over a large depth of field (see Eqs. (28) and (31)). Therefore, these beams could overcome the problems associated with conventional focused beams in nondestructive evaluation of materials.

For an initial study, we have performed pulse-echo imaging of a stainless steel block phantom with a broadband J_0 Bessel beam (the transducer used here was the same as that used for producing the broadband J_0 Bessel beam in Fig. 2 and the electrical driving pulse was given by Eq. (29))[34]. This beam was used in both transmitting and receiving of the pulse-echo imaging. A 303 stainless steel block phantom which has a speed of sound about $5.7mm/\mu s$ and 11 parallel holes (drilled through the phantom from front to back) was used as a testing object. The dimension of the phantom is 50 mm $\times$ 50 mm $\times$ 100 mm. The 11 holes were of 4 different diameters (1 hole of 10 mm, 1 hole of 5 mm, 1 hole of 2.5 mm, and 8 hole of 1 mm) and were grouped to form a resolution pattern. The resolution pattern was located around the center of the steel block in the 50 mm $\times$ 100 mm cross section plane. The distances of the center of the 10 mm hole to top surface and to a side wall of the phantom were 30 mm and 35 mm, respectively. The resolution pattern was confined in an area of 26 mm $\times$ 41 mm and the minimum lateral and axial distances between the 1 mm holes are about 2 mm.

The transducer was scanned mechanically over the top surface of the phantom which was placed at 9 distances in water (Z/D = 0.0, 0.4, 1.0, 1.4, 2.0, 2.4, 3.0, 3.4, 4.0, respectively, where Z is the distance between the surface of the transducer and the top surface of the phantom and D is the diameter of the transducer which is 50 mm). Pulse-echo images of the 50 mm $\times$ 100 mm cross section (perpendicular to the direction of the holes) of the phantom were obtained. The data acquisition window is about 50 mm (lateral) $\times$ 39.4 mm (axial). The resolution pattern of the images were resolved for all depths (Figs. 9 and 10). Line plots (see Fig. 11) through the images of an isolated 1 mm diameter hole (the right-most hole in each panel of Figs. 9 and 10 is 30 mm down from the top surface of the phantom) show that the -6 dB lateral and axial widths of the images are about 2.44 mm and 2.63 mm, respectively, throughout the depth of field of the transducer (the depth of field is about 216 mm in water).

The above study demonstrates the feasibility of applying diffraction-limited beams to nondestructive evaluation of materials. The use of diffraction-limited beams may simplify the procedures for evaluating materials of various speeds of sound.

5. DISCUSSION

5.1. Resolution and depth of field

The resolution and the depth of field of diffraction-limited beams are related to each other. For a J_0 Bessel beam, the relationship of the depth of field and the resolution is given by Eq. (28). If the scaling factor α increases, the main beamwidth of the beam will be reduced improving the lateral resolution. However, the depth of field will be reduced at the same time. For the zeroth-order X wave, the depth of field (Eq. (31)) decreases with an increase of ζ which increases the imaging resolution because of the reduced lateral beam width. In both cases, increasing the short wavelength component of the beams will increase the depth of field without affecting the main beamwidth. This is similar to that of the Rayleigh distance of a piston drive transducer. However, diffraction-limited beams maintain much larger depth of field than piston drive transducers with the same main beam width. This is of particular interest in nondestructive evaluation of materials where the speed of sound at a given frequency (or wavelength) could vary significantly from material to material. The materials of larger speed of sound will have smaller depth of field as well as larger pulse length (poor axial resolution) for a pulse of a given time duration.

Because of the large depth of field of the diffraction-limited beams, imaging systems using these beams would have a depth-invariant point spread function. If the imaging systems are linear, image restoration (deconvolution) techniques which are based on the linear shift-invariant assumption could be applied directly.[45] This would greatly simplify the procedure of deconvolution because only one point spread function is needed for deconvolving the entire image (Fig. 12). We report here such a study in which a Wiener filter[45] was used for the deconvolution. The point spread function used was the RF image of the point target of a phantom (commercial RMI413A tissue equivalent phantom which is made of tissue mimicking materials with an attenuation coefficient of 0.7 dB/MHz/cm and a group of Nylon point targets) which is indicated with the arrow sign, "↖". The ratio of the spectrum intensity of noise versus the spectrum intensity of the object (the phantom) was assumed to be a constant and equal to 1 percent of the maximum of the square of the modulus of the Fourier transform of the point spread function of the system in the Wiener filter. After deconvolution, the sidelobes of the point targets of the phantom are reduced and both lateral and axial resolutions are enhanced (Fig. 12). Deconvolution was also done for images of other objects. The results showed approximately a 10 dB reduction of sidelobes was obtainable.[33] In addition to the two-dimensional deconvolution, one-dimensional deconvolution could also be used to speed up the processing for restoration of images obtained using diffraction-limited beams.[35]

5.2. Sidelobes

The sidelobes are essential for the diffraction-limited beams. It is the sidelobes that construct the diffraction-limited beams as they propagate. Therefore, for theoretical diffraction-limited beams, there should be an infinite amount of energy on the sidelobes to keep the beams from spreading forever. This

can be seen from Fig. 3 and Fig. 6 where the sidelobe levels are similar for the J_0 Bessel beams and X waves. The sidelobes will degrade contrast of medical imaging and cause artifacts in nondestructive evaluation of materials. For biological tissue characterization, the sidelobes increase the effective sampling volume. To reduce the effects of the sidelobes of the diffraction-limited beams in medical pulse-echo imaging, the diffraction-limited beams could be used in transmitting and conventional dynamically focused beams used in receiving. Simulation and experiment on a tissue equivalent contrast-detail phantom showed that high-resolution, high-contrast, and high-frame rate imaging would be possible with a pulse-echo imaging system which combines the diffraction-limited beams and the conventional dynamic focused beams.[31,32] The image restoration techniques mentioned above could also be used for suppressing the sidelobes, especially, for some applications on nondestructive evaluation of materials where the condition of shift-invariance of the point spread function is approximately satisfied. The bigger sampling volume caused by the sidelobes of the diffraction-limited beams will limit biological tissue parameter estimation to those regions where the distributions of parameters are relatively uniform.

5.3. Sensitivity

Unlike the focused beams where the intensity of the beams is enhanced at the focus, the intensity of diffraction-limited beams is relatively uniform throughout the depth of field. This would present a continuous intensity drop of the diffraction-limited beams in attenuating media such as biological soft tissues. Therefore, for a system of a given signal-to-noise ratio, the penetration depth of the diffraction-limited beams could be shorter. However, the difference between the depth of penetration of the diffraction-limited beams and the conventional focused beams might not be very big in medical imaging. This is because focused beams of a fixed focal length will be out of focus quickly with depth which reduces the intensity dramatically. At focus the intensity enhancement of focused beams decreases with the increase of the focal length for a given aperture size. Bigger aperture sizes are usually avoided due to the phase aberration of biological soft tissues.

Lack of intensity enhancement of the diffraction-limited beams results in the intensity of the beams being highest at surface of the transducers. This could cause heating of skin. To avoid possible skin heating, the intensity of the central portion of the beams can be set to zero reshaping the beams to increase their intensity gradually with depth. After certain distances, say a few centimeters (depending on how large the central area is set to zero), the diffraction-limited beams are recovered (the diffraction-limited beams in farther distances are formed mainly by the outer rings). This method trades off the peak intensity reduction with range of the blind area near the surface of the transducer.[30]

5.4. Attenuation and phase aberration of media

In medical imaging and tissue characterization, the media (biological soft tissues) are highly attenuating and could have strong phase aberration. The theoretical diffraction-limited beams are derived originally from the loss-free, isotropic/homogeneous wave equation, therefore, their applications are subject to perturbations of the media. A preliminary study of phase aberration effects of the diffraction-

limited beams was performed and the results showed that the effects are similar to those of conventional focused beams.[23] Further comparison will be carried out with images obtained with a real-time scanner.

5.5. Other diffraction-limited beams

Because the function $f(s)$ in Eq. (2) is free to chose, an infinite number of new diffraction-limited beams could be obtained. The properties of the new diffraction-limited beams and the differences between these beams and the X waves or the Bessel beams has yet to be studied.

5.6. Other applications

In addition to ultrasonics, applications of the diffraction-limited beams in other wave related fields such as, microwaves, optics and electromaganetics are possible. Diffraction-limited beams share some properties of Ziolkowski's localized waves and should likewise be applicable in electromagnetic energy transmission, private communications and military system.[16]

6. CONCLUSION

The extension of diffraction-limited beams to n-dimensional space could have theoretical importance. This generalization will broaden our view of such solutions. Preliminary studies of diffraction-limited beams using both simulation and experiment show that these novel beams could be useful in medical imaging and tissue characterization because of their large depth of field and propagation-invariant property. They would also be applicable in nondestructive evaluation of materials where their main beamwidth (lateral resolution) is independent of the speed of sound of the materials inspected. Further applications of these beams depend on trade offs among depth of field, sidelobes, resolution and energy efficiency.

7. ACKNOWLEDGMENTS

The authors thank Randall R. Kinnick for his development of electronics used in the experiments. The authors also appreciate the secretarial assistance of Elaine C. Quarve and the graphic assistance of Christine A. Welch. This work was supported in part by grants CA 43920 and CA54212 from the National Institutes of Health.

8. REFERENCES

1. J. Durnin, "Exact solutions for nondiffracting beams. I. The scalar theory," *J. Opt. Soc. Am.*, vol. 4, no. 4, pp. 651–654, 1987.
2. J. Durnin, J. J. Miceli, Jr., and J. H. Eberly, "Diffraction-free beams," *Phys. Rev. Lett.*, vol. 58, no. 15, pp. 1499–1501, April 13, 1987.

3. G. Indebetow, "Nondiffracting optical fields: some remarks on their analysis and synthesis," *J. Opt. Soc. Am. A*, vol. 6, no. 1, pp. 150–152, Jan., 1989.
4. F. Gori, G. Guattari, and C. Padovani, "Model expansion for J_0-correlated Schell-model sources," *Optics Commun.*, vol. 64, no. 4, pp. 311–316, Nov. 15, 1987.
5. K. Uehara and H. Kikuchi, "Generation of near diffraction-free laser beams," *Appl. Physics B*, vol. 48, pp. 125–129, 1989.
6. L. Vicari, "Truncation of nondiffracting beams," *Optics Commun.*, vol. 70, no. 4, pp. 263–266, Mar. 15, 1989.
7. M. Zahid and M. S. Zubairy, "Directionally of partially coherent Bessel-Gauss beams," *Optics Commun.*, vol. 70, no. 5, pp. 361–364, April 1, 1989.
8. S. Y. Cai, A. Bhattacharjee, and T. C. Marshall, "'Diffraction-free' optical beams in inverse free electron laser acceleration," *Nuclear Instruments and Methods in Physics Research, Section A: Accelerators, Spectrometers, Detectors, and Associated Equipment*, vol. 272, no. 1–2, pp. 481–484, Oct., 1988.
9. J. B. Brittingham, "Focus wave modes in homogeneous Maxwell's equations: transverse electric mode," *J. Appl. Phys.*, vol 54, no. 3, pp. 1179–1189, 1983.
10. R. W. Ziolkowski, "Exact solutions of the wave equation with complex source locations," *J. Math. Phys.*, vol. 26, no. 4, pp. 861–863, April, 1985.
11. R. W. Ziolkowski, D. K. Lewis, and B. D. Cook, "Evidence of localized wave transmission," *Phys. Rev. Lett.*, vol. 62, no. 2, pp. 147–150, Jan. 9, 1989.
12. R. W. Ziolkowski and D. K. Lewis, "Verification of the localized wave transmission effect," *J. Appl. Phys.*, vol. 68, no. 12, pp. 6083–6086, Dec. 15, 1990.
13. E. Heyman, B. Z. Steinberg, and L. B. Felsen, "Spectral analysis of focus wave modes," *J. Opt. Soc. Am. A*, vol. 4, no. 11, pp. 2081–2091, Nov., 1987.
14. A. M. Shaarawi, I. M. Besieris, and R. W. Ziolkowski, "Localized energy pulse train launched from an open, semi-infinite, circular waveguide," *J. Appl. Phys.*, vol. 65, no. 2, pp. 805–813, 1989.
15. I. M. Besieris, A. M. Shaarawi, and R. W. Ziolkowski, "A bidirectional traveling plane wave representation of exact solutions of the scalar wave equation," *J. Math. Phys.*, vol. 30, no. 6, pp. 1254–1269, 1989.
16. R. W. Ziolkowski, "Localized transmission of electromagnetic energy," *Phys. Rev. A.*, vol. 39, no. 4, pp. 2005–2033, Feb. 15, 1989.
17. J. V. Candy, R. W. Ziolkowski, and D. K. Lewis, "Transient waves: reconstruction and processing," *J. Acoust. Soc. Am.*, vol. 88, no. 5, pp. 2248–2258, Nov., 1990.
18. J. V. Candy, R. W. Ziolkowski, and D. K. Lewis, "Transient wave estimation: a multichannel deconvolution application," *J. Acoust. Soc. Am.*, vol. 88, no. 5, pp. 2235–2247, Nov., 1990.
19. R. W. Ziolkowski, A. M. Shaarawi and I. M. Besieris, "A space-time representation of a massive, relativistic, spin zero particle,"*Nuclear Physics B (Proceeding Suppl.)*, North-Holland, Amsterdam, vol. 6, pp. 255–258, March, 1989.
20. A. M. Shaarawi, I. M. Besieris, and R. W. Ziolkowski, "A novel approach to the synthesis of nondispersive wave packet solutions to the Klein-Gordon and Dirac equations," *J. Math. Physics*, vol. 31, no. 10, pp. 2511–2519, Oct., 1990.

21. D. K. Hsu, F. J. Margetan, and D. O. Thompson, "Bessel beam ultrasonic transducer: fabrication method and experimental results," *Appl. Phys. Lett.*, vol. 55, no. 20, pp. 2066–2068, Nov. 13, 1989.

22. J. A. Campbell and S. Soloway, "Generation of a nondiffracting beam with frequency independent beam width," *J. Acoust. Soc. Am.*, vol. 88, no. 5, pp. 2467–2477, Nov., 1990.

23. Jian-yu Lu and J. F. Greenleaf, "Ultrasonic nondiffracting transducer for medical imaging," *IEEE Trans. Ultrason., Ferroelec., Freq. Contr.*, vol. 37, no. 5, pp. 438–447, Sept., 1990.

24. Jian-yu Lu, and J. F. Greenleaf, "Evaluation of a nondiffracting transducer for tissue characterization," [IEEE 1990 Ultrasonics Symposium, Honululu, HI, U.S.A., Dec. 4–7, 1990], *IEEE 1990 Ultrason. Symp. Proc.*, 90CH2938–9, vol. 2, pp. 795–798, 1990.

25. Jian-yu Lu and J. F. Greenleaf, "Pulse-echo imaging using a nondiffracting beam transducer," *Ultrasound Med. Biol.* vol. 17, no. 3, pp. 265–281, May, 1991.

26. Jian-yu Lu and J. F. Greenleaf, "Theory and acoustic experiments of nondiffracting X waves," [IEEE 1991 Ultrasonics Symposium, Lake Buena Vista, FL, U.S.A., Dec. 8–11, 1991], *IEEE 1991 Ultrason. Symp. Proc.*, 91CH3079–1, vol. 2, pp. 1155–1159, 1991.

27. Jian-yu Lu and J. F. Greenleaf, "Nondiffracting X waves — exact solutions to free-space scalar wave equation and their finite aperture realizations," *IEEE Trans. Ultrason., Ferroelec., Freq. Contr.*, vol. 39, no. 1, pp. 19–31, Jan., 1992.

28. Jian-yu Lu and J. F. Greenleaf, "Experimental verification of nondiffracting X waves," *IEEE Trans. Ultrason., Ferroelec., Freq. Contr.*, vol. 39, no. 3, pp. 441–446, May, 1992.

29. Jian-yu Lu and J. F. Greenleaf, "A computational and experimental study of nondiffracting transducer for medical ultrasound," [Fifteenth International Symposium on Ultrasonic Imaging and Tissue Characterization, Arlington, VA, June 11–13, 1990], *Ultrason. Imaging*, vol. 12, no. 2, pp.146–147, April, 1990 (abs).

30. Jian-yu Lu and J. F. Greenleaf, "Effect on J_0 nondiffracting beam of deleting central elements of J_0 annular array transducer," [Sixteenth International Symposium on Ultrasonic Imaging and Tissue Characterization, Arlington, VA June 3–5, 1991], *Ultrason. Imaging*, vol. 13, no. 2, p. 203, April, 1991 (abs).

31. Jian-yu Lu and J. F. Greenleaf, "Simulation of imaging contrast of nondiffracting beam transducer," [AIUM 35th Annual Convention, Atlanta, GA, February 24-27, 1991], *J. Ultrasound Med.*, vol. 10, no. 3, (Suppl.), p. S4, March, 1991 (abs).

32. Jian-yu Lu and J. F. Greenleaf, "Experiment of imaging contrast of J_0 Bessel nondiffracting beam transducer," [AIUM 36th Annual Convention, San Diego, CA, March 8–11, 1992], *J. Ultrasound Med.*, vol. 11, no. 3, (Suppl.), p. S43, March, 1992 (abs).

33. Jian-yu Lu and J. F. Greenleaf, "Sidelobe reduction of nondiffracting pulse-echo images by deconvolution," [Seventeenth International Symposium on Ultrasonic Imaging and Tissue Characterization, Arlington, VA, June 1–3, 1992], *Ultrason. Imaging*, vol. 14, no. 2, p. 203, April, 1992 (abs).

34. Jian-yu Lu and J. F. Greenleaf, "Nondestructive evaluation of materials with a J_0 Bessel transducer," [Seventeenth International Symposium on Ultrasonic Imaging and Tissue Characterization, Arlington, VA, June 1–3, 1992], *Ultrason. Imaging*, vol. 14, no. 2, pp. 203–204, April, 1992 (abs)

35. M. Fatemi and M. A. Arad, "Ultrasonic nondiffracting beam image formation and restoration," [IEEE 1991 Ultrasonics Symposium, Lake Buena Vista, FL, U.S.A., Dec. 8–11, 1991], *IEEE 1991 Ultrason. Symp. Proc.*, 91CH3079–1, vol. 2, pp. 1305–1308, 1991.
36. F. John, *Partial Differential Equations* New York: Springer-Verlag, 1982.
37. P. M. Morse and H. Feshbach, *Methods of Theoretical Physics,* Part I, New York: McGraw-Hill Book Company, Inc., 1953.
38. I. S. Gradshteyn and I. M. Ryzhik, *Table of Integrals, Series, and Products,* Corrected and Enlarged Edition. New York: Academic Press, 1980, ch. 17.
39. M. S. Patterson and F. S. Foster, "Acoustic fields of conical radiators," *IEEE Trans. Sonics Ultrason.*, SU-29, no. 2, pp. 83–92, March, 1982.
40. E. L. Madsen, M. F. Insana, and J. A. Zagzebski, "Method of data reduction for accurate determination of acoustic backscatter coefficients," *J. Acoust. Soc. Am.*, vol. 76, no. 3, pp. 913–923, Sept., 1984.
41. M. F. Insana, E. L. Madsen, T. J. Hall, and J. A. Zagzebski, "Tests of the accuracy of a data reduction method for determination of acoustic backscatter coefficients," *J. Acoust. Soc. Am.*, vol. 79, no. 5, pp. 1230–1236, May, 1986.
42. T. J. Hall, E. L. Madsen, J. A. Zagzebski, and E. J. Boote, "Accurate depth-independent determination of acoustic backscatter coefficients with focused transducers," *J. Acoust. Soc. Am.*, vol. 85, no. 6, pp. 2410–2416, June, 1989.
43. J. Krautkramer and H. Krautkramer, *Ultrasonic testing of materials,* Third Edition, New York: Springer-Verlag, 1983.
44. A. V. Oppenheim and R. W. Schafer, *Digital Signal Processing,* New Jersey: Prentice-Hall, Inc., 1975, ch. 5.
45. A. Rosenfeld and A. C. Kak, *Digital Picture Processing*, New York: Academic Press, 1982.

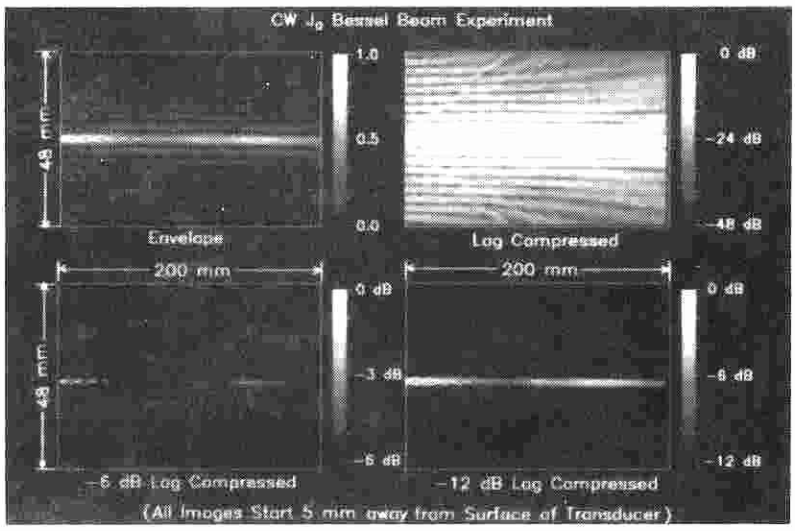

Figure 1. Experimentally measured piecewise approximated continuous wave (CW) J_0 Bessel beam in water. It was produced with a 10–element, 2.5 MHz and 50 mm diameter annular array transducer. Each annular element of the transducer approximated a lobe of the Bessel function $J_0(\alpha r)$ with the scaling factor, $\alpha = 1202.45m^{-1}$. The amplitude of acoustic pressure produced by each element is proportional to the maximum absolute value of each lobe of the Bessel function. The magnitude (envelope) of the same measured field was displayed as 4 panels with linear, log compressed, -6 dB clipped log compressed, and -12 dB clipped log compressed formats, respectively. All panels begin 5 mm away from the surface of the transducer and the dimension of the panels is 48 mm $\times$ 200 mm. [Modified with permission from 23]

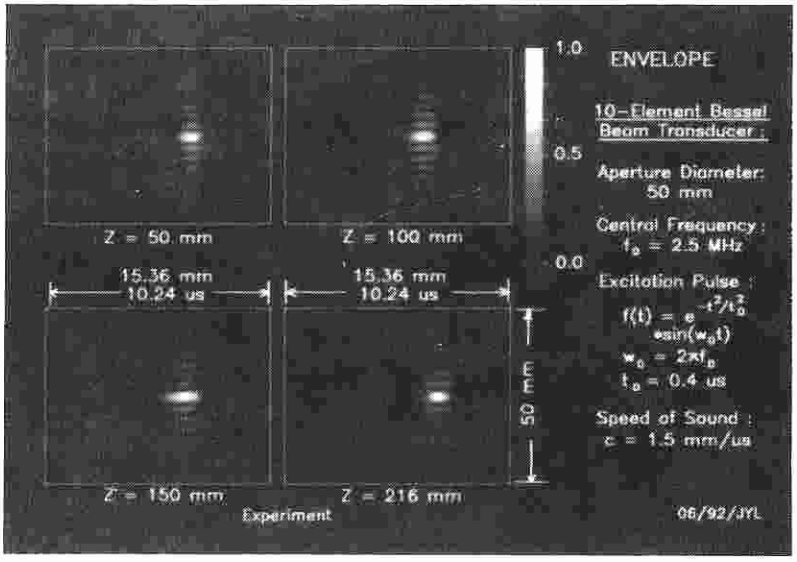

Figure 2. Pulse wave (PW) experiment of the J_0 Bessel beam in water. The transducer used to produce the pulses was the same as that in Fig. 1 and the drive function was given by Eq. (29). The pulses were measured at four distances away from the surface of the transducer: Z = 50 mm, 100 mm, 150 mm and 216 mm, respectively, and linear envelopes of the RF pulses were displayed. The pulses were measured in a plane along their axial axes (the axial direction of the pulses is in parallel with the lateral direction of the paper). The panel size is 50 mm $\times$ 10.24 μs (15.36 mm). [Modified with permission from 23]

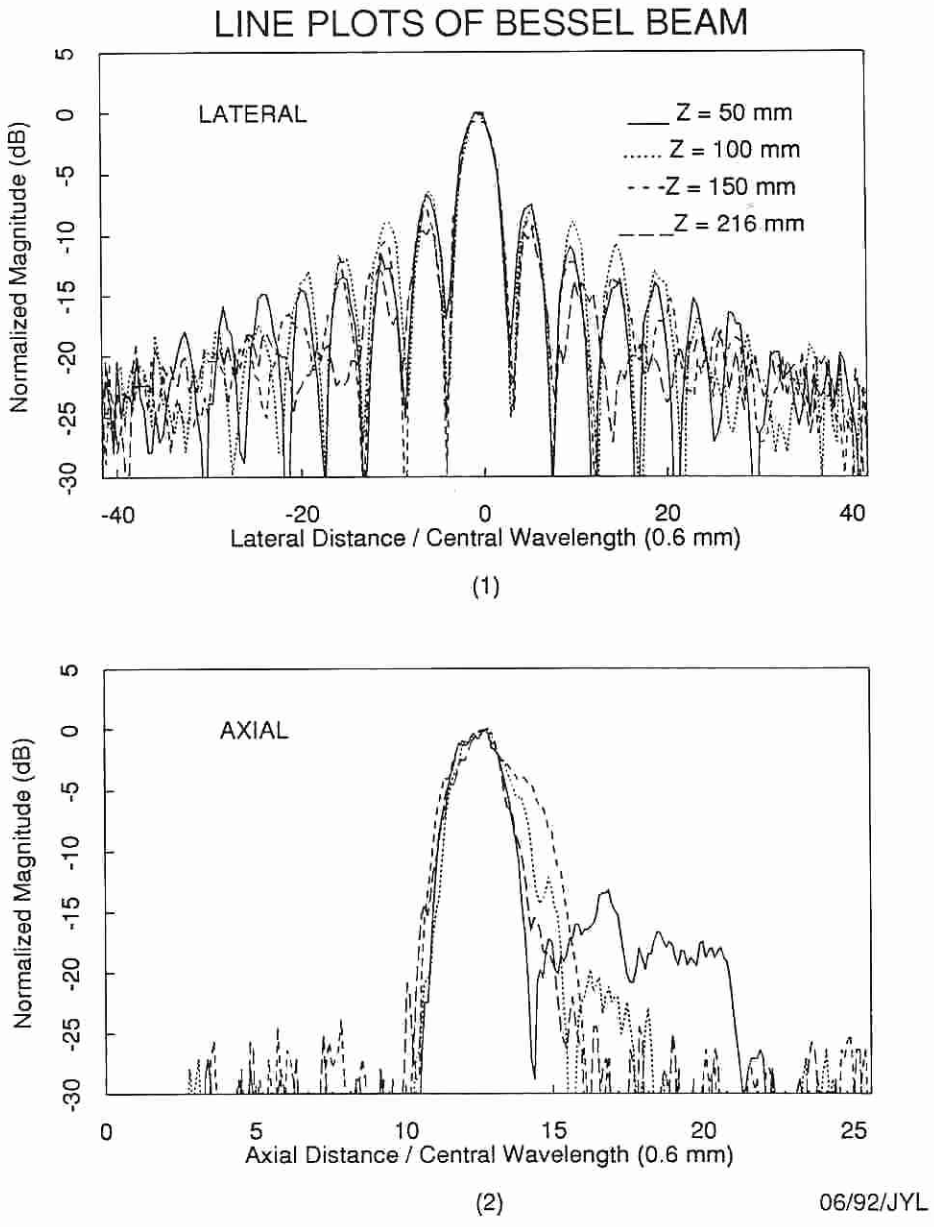

Figure 3. (1) Lateral and (2) axial line plots of the pulses in Fig. 2 at four depths through the peaks of pulses. Full, dotted, dashed and long dashed lines represent the plots at distances of 50 mm, 100 mm, 150 mm and 216 mm, respectively. The lateral axis of the plots represents lateral distance over central wavelength (0.6 mm in water) and vertical axis is normalized magnitude in dB scale.

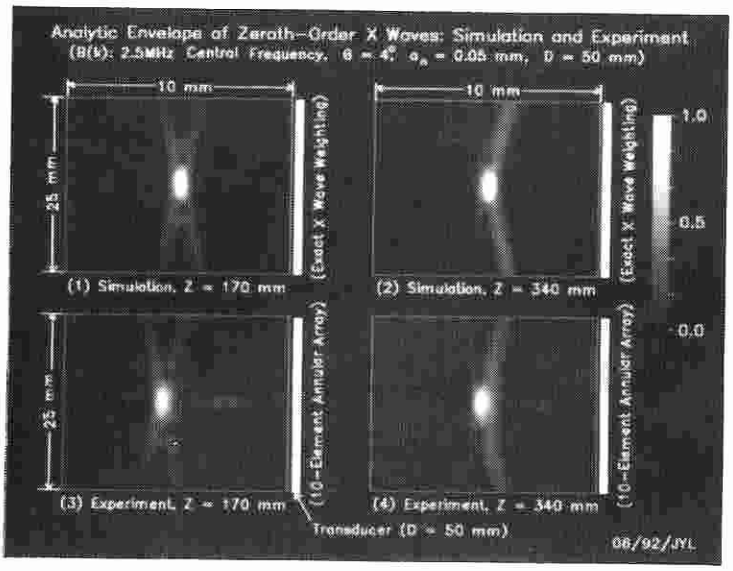

Figure 4. Panels (1) and (2): Computer simulations of the zeroth-order, band-limited, diffraction-limited, X wave at distances Z = 170 mm and 340 mm, respectively, away from the surface of the transducer. The transducer used was an annular array and was the same as used in Figs. 1 and 2. Exact X wave aperture weighting and broadband X wave pulse drive for the transducer were assumed. The transmitting transfer function of the transducer was assumed to be the Blackman window function peaked at 2.5 MHz and with -6 dB bandwidth around 2.1 MHz. Panels (3) and (4): Experimental results corresponding to the simulations in (1) and (2), respectively. The panel size is 25 mm (height) $\times$ 10 mm (width), and the parameters a_0 and ζ are 0.05 mm and 4°, respectively. The linear analytic envelope of the real part of the X waves is displayed for all panels. [Modified with permission from 28]

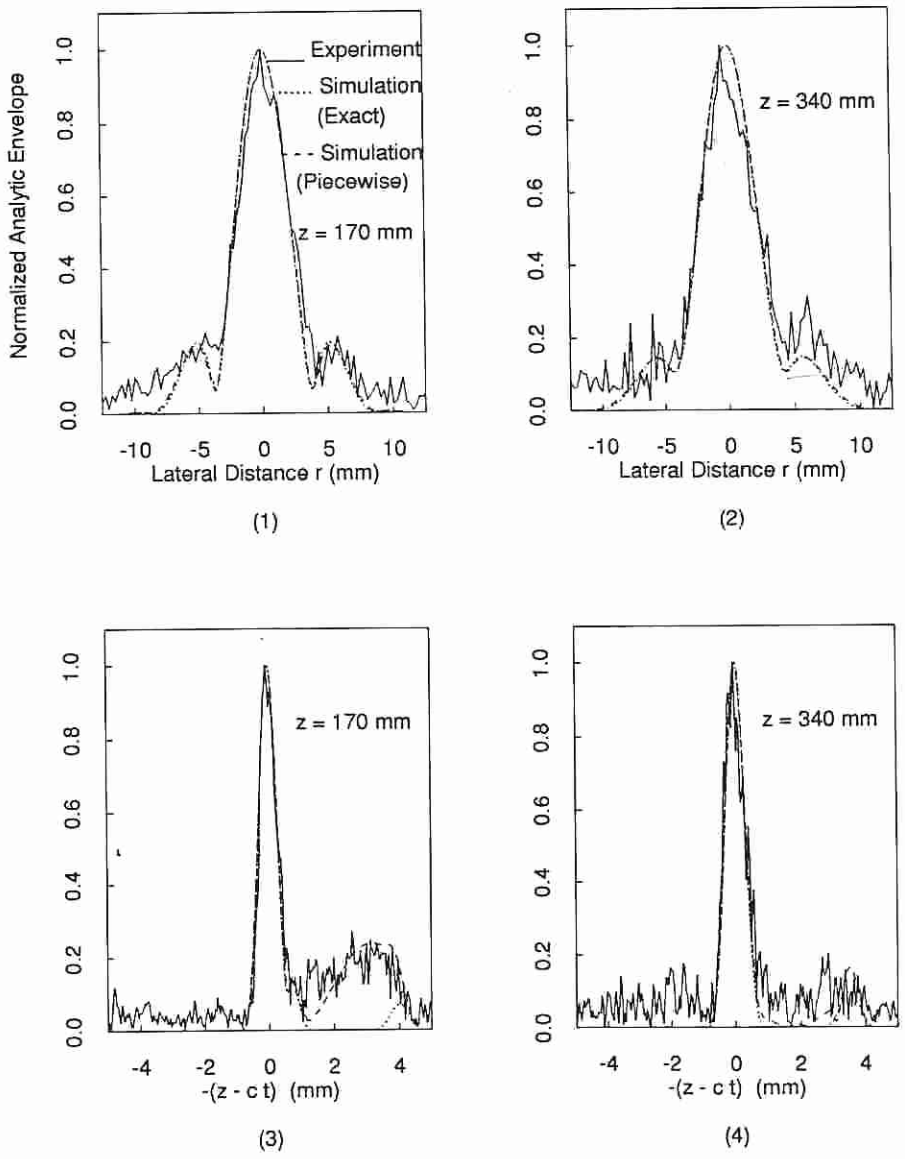

Figure 5. Lateral ((1) and (2)) and axial ((3) and (4)) line plots of the zeroth-order X waves in Fig. 4 through the wave peaks at distances Z = 170 mm (Panels (1) and (3)) and Z = 340 mm (Panels (2) and (4)). Full, dotted and dashed lines correspond to experiment, simulation with an exact X wave aperture weighting (continuous aperture weighting) and simulations with a piecewise (segmenting transducer into 10 annuli) X wave aperture weighting, respectively. [Reproduced with permission from 28]

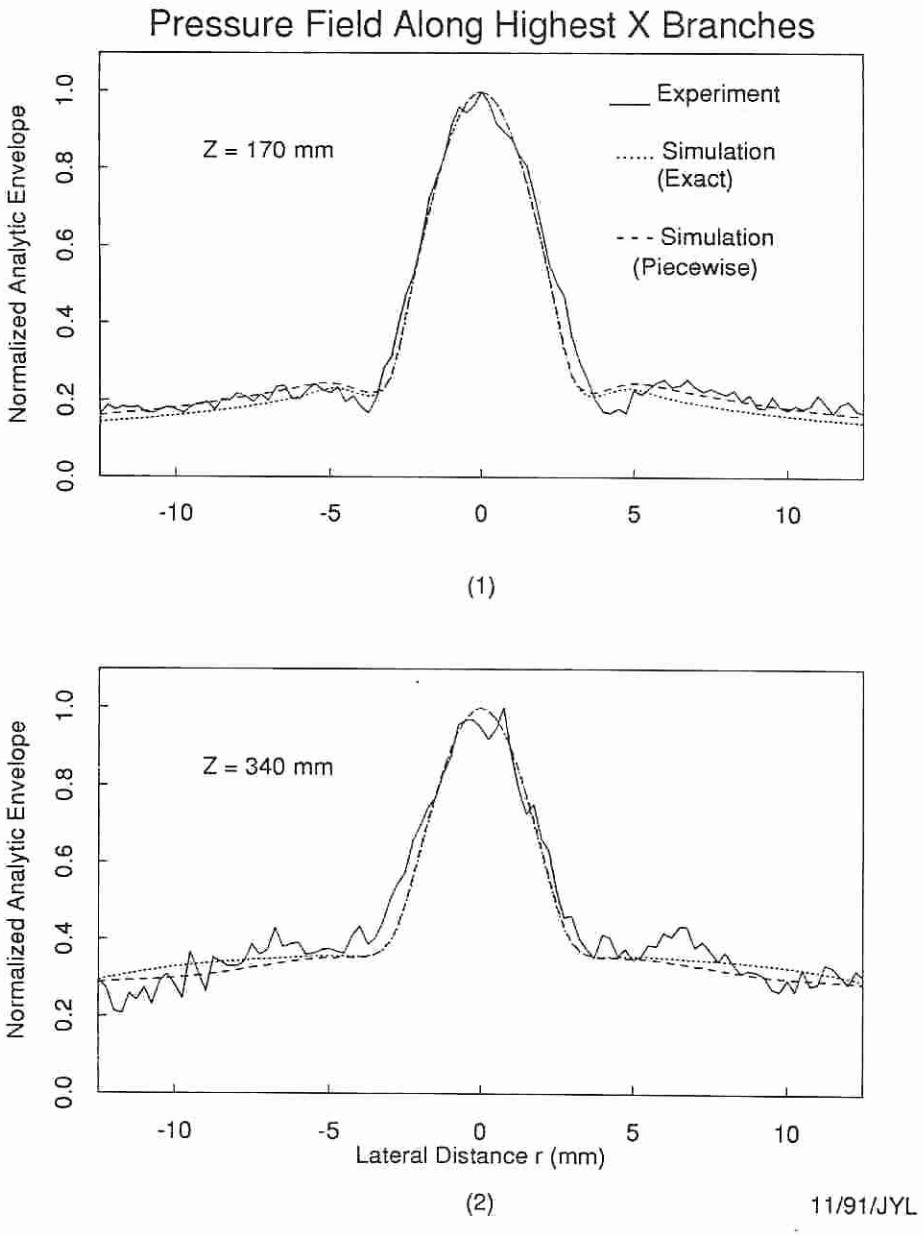

Figure 6. Line plots along the largest X branches of the X waves in Fig. 4 at distance (1) Z = 170 mm and (2) 340 mm. Full, dotted and dashed lines have the same meaning as those in Fig. 5. [Reproduced with permission from 26]

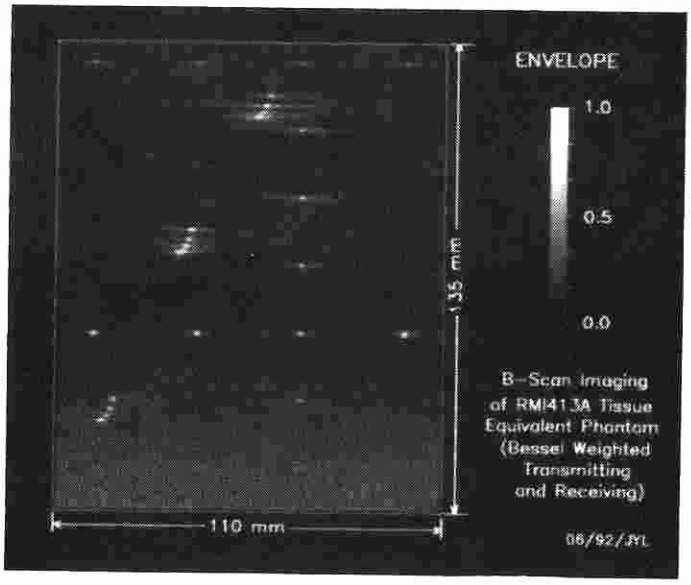

Figure 7. B-scan image of a commercial RMI413A tissue equivalent phantom obtained with a J_0 Bessel beam in both transmitting and receiving. The transducer used was the same as that used for producing the pulses in Fig. 2 and was placed 30 mm above the top line reflectors. The panel size of the image is 110 mm $\times$ 135 mm. Linear analytic envelope is displayed. [Modified with permission from 25]

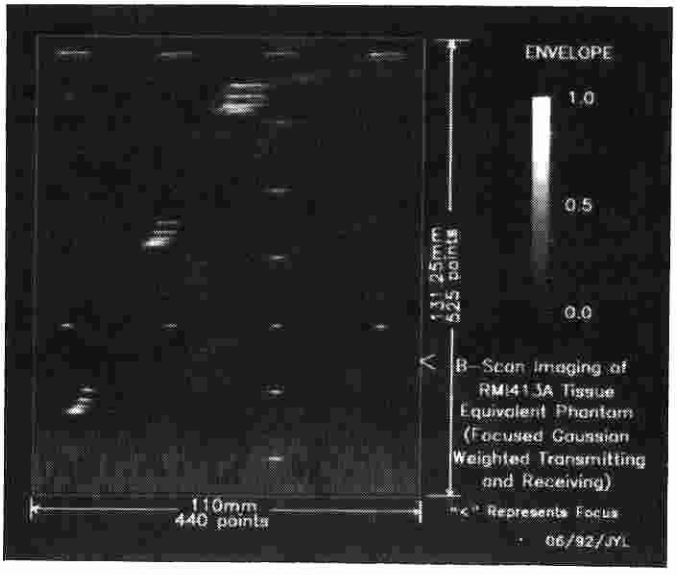

Figure 8. Same format as Fig. 7 except that a conventional focused Gaussian beam was used (focal length is 120 mm and full width at half maximum of the beam at the surface of the transducer is 25 mm). "<" sign represents the depth where both the transmitting and receiving beams are focused and the panel size is 110 mm $\times$ 131.25 mm. [Modified with permission from 25]

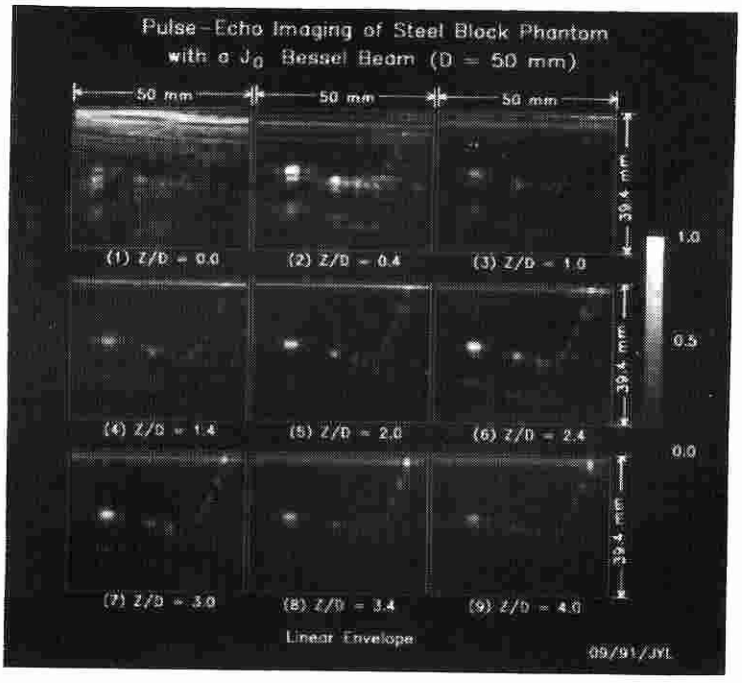

Figure 9. Envelopes of experimentally measured B-scan images of a cross section of a stainless steel phantom. Panels (1) to (9) correspond to images obtained at Z/D = 0.0, 0.4, 1.0, 1.4, 2.0, 2.4, 3.0, 3.4, and 4.0, respectively (Z and D are axial distance from the transducer surface to the top surface of the phantom and the diameter of the transducer, respectively, and D = 50 mm). Panel size is 50 mm (width) × 39.4 mm (height) which represents a window that avoids strong multiple reflections between the flat transducer surface and the phantom, and strong reflection of the water-phantom interface. The gray level of each panel is normalized to its maximum. [Reproduced with permission from Jian-yu Lu and J. F. Greenleaf, "Nondestructive evaluation of materials with a diffraction-limited beam," *Ultrason. Imaging,* Submitted, 1992]

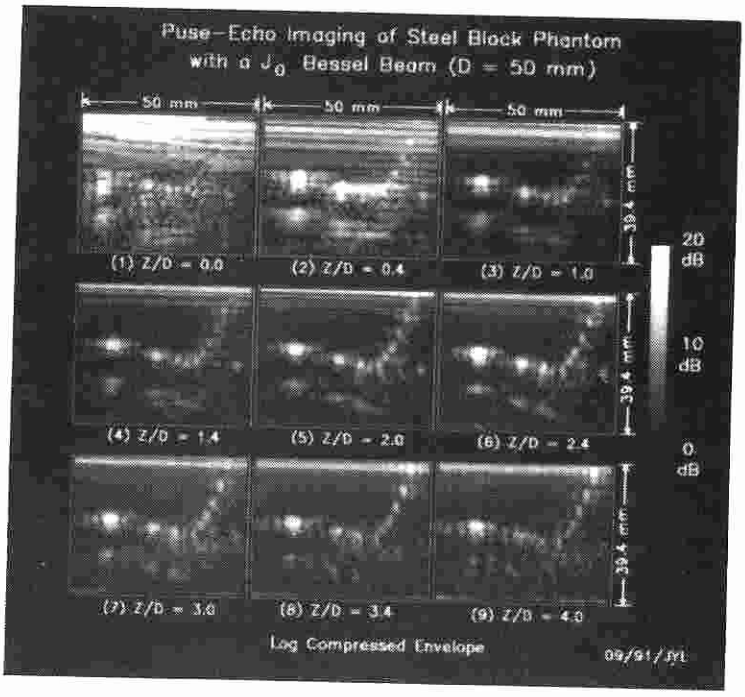

Figure 10. The same as figure 9 except that the images are log compressed. The brightest and darkest pixels of the images are 20 dB and 0 dB, respectively. [Reproduced with permission from Jian-yu Lu and J. F. Greenleaf, "Nondestructive evaluation of materials with a diffraction-limited beam," *Ultrason. Imaging,* Submitted, 1992]

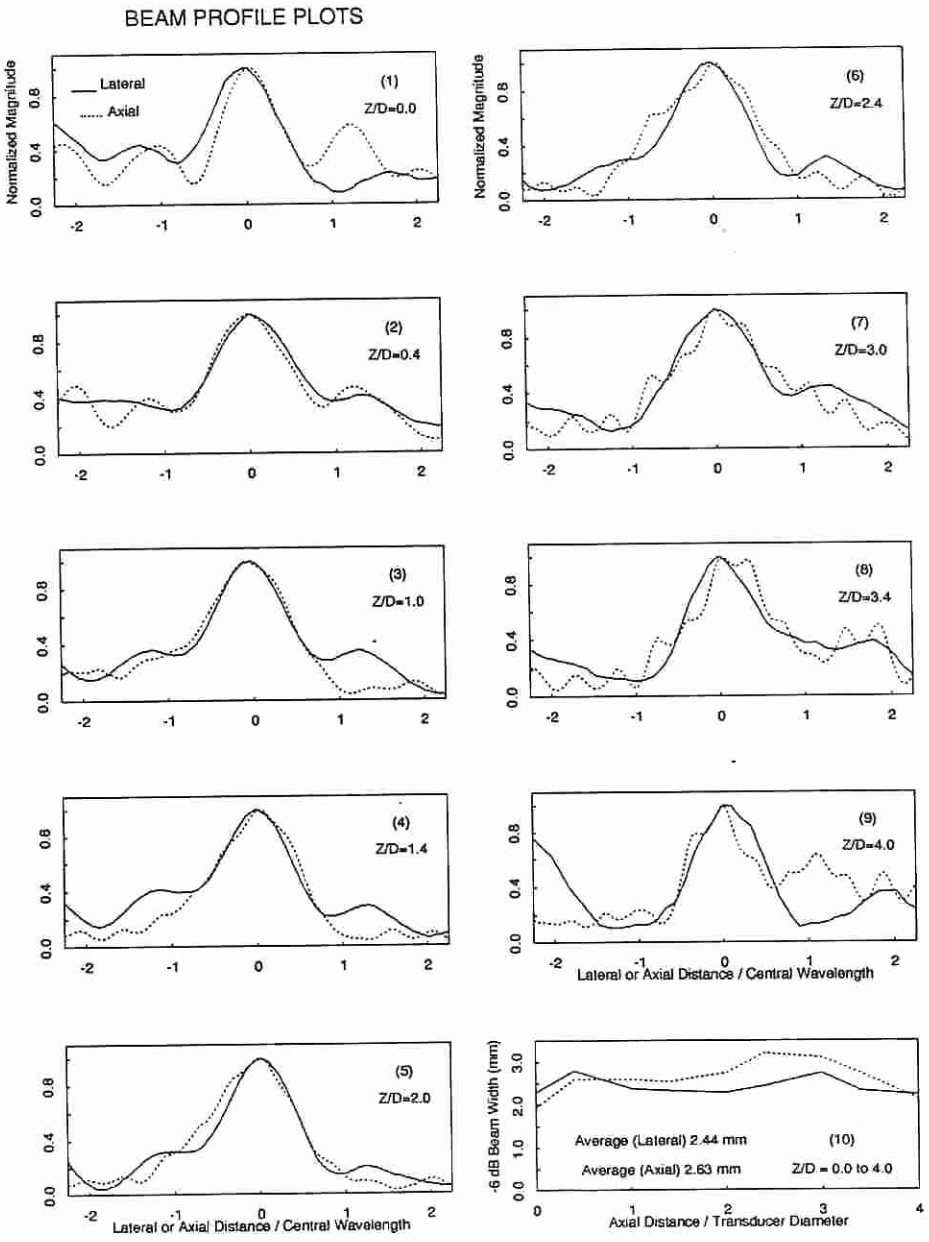

Figure 11. Lateral (full lines) and axial (dotted lines) line plots of the images of the right-most $\phi 1$ mm hole in Figs. 9 and 10 (30 mm down from the top surface of the phantom) at different Z/D values (Panels (1) to (9)). Panel (10) is the -6 dB width of the lateral and axial line plots of the images versus the Z/D values. The central wavelength in steel is about 2.28 mm and transducer diameter is 50 mm. [Reproduced with permission from Jian-yu Lu and J. F. Greenleaf, "Nondestructive evaluation of materials with a diffraction-limited beam," *Ultrason. Imaging*, Submitted, 1992]

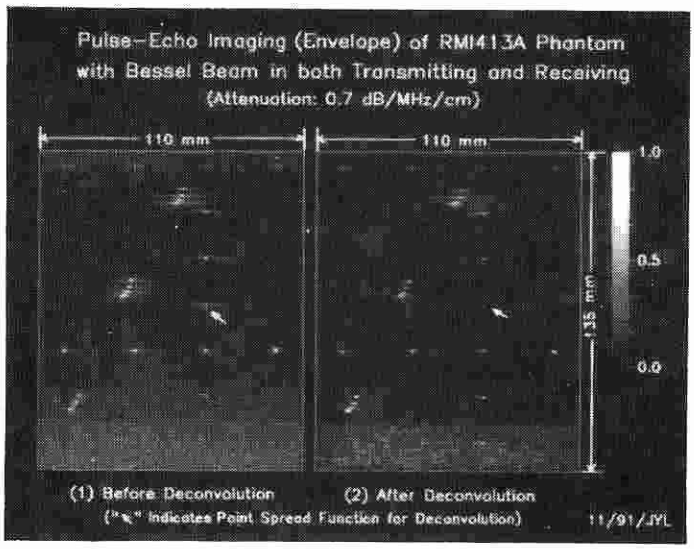

Figure 12. Deconvolution of an image obtained with a J_0 Bessel beam using the Wiener filtering technique. Only one point spread function of the imaging system was used for deconvolution of the entire image. Panels (1) and (2) are images before and after the deconvolution, respectively, and Panel (1) is reproduced from Fig. 7 for a better comparison. "↖" sign indicates the point target whose RF image was used as the point spread function of the imaging system. Envelope of the RF images were displayed. The panel size of the images is 110 mm × 135 mm. The targets of the phantom are surrounded with tissue mimicking material with an attenuation coefficient of 0.7 dB/MHz/cm. The central frequency of the J_0 Bessel beam is 2.5 MHz and aperture diameter is 50 mm.